Pulmonary Circulation

WILEY

PVRi | Pulmonary Circulation Open Access

RESEARCH ARTICLE OPEN ACCESS

Multiscale Three-Dimensional Evaluation and Analysis of Murine Lung Vasculature From Macro- to Micro-Structural Level

Birger Tielemans[1] | Nora F. Marain[2] | Axelle Kerstens[3] | Nicolas Peredo[3] | Montserrat Coll-Lladó[4] | Nicola Gritti[4] | Perrine de Villemagne[5] | Paul Dorval[5] | Vincent Geudens[2] | Michaela Orlitová[6] | Sebastian Munck[3] | Bartosz Leszczyński[7] | Jim Swoger[4] | Greetje Vande Velde[1]

[1]Department of Imaging and Pathology, Biomedical MRI, KU Leuven, Leuven, Belgium | [2]Department of Chronic Diseases and Metabolism, Laboratory of Respiratory Diseases and Thoracic Surgery (BREATHE), KU Leuven, Leuven, Belgium | [3]VIB Bio Imaging Core, KU Leuven, Department of Neurosciences, Leuven Brain Institute, Leuven, Belgium | [4]European Molecular Biology Laboratory (EMBL) Barcelona, Barcelona, Spain | [5]Kaer Labs, Nantes, France | [6]Department of Cardiovascular Sciences, KU Leuven, Department of Thoracic Surgery, University Hospitals Leuven, Leuven, Belgium | [7]Department of Medical Physics, M. Smoluchowski Institute of Physics, Faculty of Physics, Astronomy and Applied Computer Science, Jagiellonian University, Kraków, Poland

Correspondence: Birger Tielemans (birger.tielemans@kuleuven.be)

Received: 26 July 2024 | **Revised:** 29 October 2024 | **Accepted:** 23 December 2024

Funding: This project was funded by departmental grants received in 2022 and 2023 by the Department of Imaging and Pathology, KU Leuven. A FWO fellowship "short stay abroad" (FWO–K222922N) and Christian Boulin fellowship (EMBL) were received by B.T.

Keywords: 3D visualization and evaluation | microcomputed tomography | optical imaging | pulmonary vasculature | serial block face imaging

ABSTRACT

The pulmonary vasculature plays a pivotal role in the development and progress of chronic lung diseases. Due to limitations of conventional two-dimensional histological methods, the complexity and the detailed anatomy of the lung blood circulation might be overlooked. In this study, we demonstrate the practical use of optical serial block face imaging (SBFI), ex vivo microcomputed tomography (micro-CT), and nondestructive optical tomography for visualization and quantification of the pulmonary circulation's 3D architecture from macro- to micro-structural levels in murine lung samples. We demonstrate that SBFI can provide rapid, cost-effective, and label-free visualization of mouse lung macrostructures and large pulmonary vessels. Micro-CT offers high-resolution imaging and captures microvascular and (pre)capillary structures, with microstructural quantification. Optical microscopy techniques such as optical projection tomography (OPT) and light sheet fluorescence microscopy, allows noninvasive, mesoscopic imaging of optically cleared mouse lungs, still enabling 3D microscopic reconstruction down to the precapillary level. By integrating SBFI, micro-CT, and nondestructive optical microscopy, we provide a framework for detailed and 3D understanding of the pulmonary circulation, with emphasis on vascular pruning and rarefaction. Our study showcases the applicability and complementarity of these techniques for organ-level vascular imaging, offering researchers flexibility in selecting the optimal approach based on their specific requirements. In conclusion, we propose 3D-directed approaches for a detailed whole-organ view on the pulmonary vasculature in health and disease, to advance our current knowledge of diseases affecting the pulmonary vasculature.

The lung is a complex organ in which a network of pulmonary arteries aligns with airway structures and alveoli, enabling efficient gas exchange for the human body. Interruption of this homeostasis due to infections, smoking, or environmental

factors, in combination with each individual's genetic predisposition, may result in acute or chronic lung diseases. When investigating the pathological development and quantifying therapeutic efficacy, it is essential to study the complete organ, including its vasculature [1]. Current studies of lung diseases primarily affecting the airways, focus on the airway system and often neglect the structural role of the pulmonary vasculature. However, the role of the pulmonary vasculature throughout the development and maintenance of lung homeostasis is of utter importance [2, 3]. Many lung diseases, such as chronic obstructive pulmonary disease (COPD) [4], and pulmonary hypertension [5], display major endothelial remodeling and pruning, highlighting the involvement of the endothelium and pulmonary vasculature in different chronic lung diseases. Nevertheless, studies focusing on the visualization and analysis of the global structural changes of the lung vasculature during different lung diseases are missing, but nevertheless indispensable towards understanding the role of the pulmonary circulation in health and disease.

In clinical situations, different imaging modalities, such as chest X-ray, computed tomography (CT), CT angiography and lung scintigraphy are generally used and provide crucial spatial information about patients' lungs and might be accompanied by histopathological analysis on lung biopsies. In experimental research, ex vivo 2-dimensional (2D) histopathologic analysis remains the gold standard for evaluating morphology, morphometry, and lung pathologies at the microscopic scale [6, 7]. However, this approach lacks 3D information on spatial heterogeneity and complexity of airways and vascular networks [8]. As a result, preclinical researchers need reproducible, quantitative 3D techniques to visualize and analyze pulmonary structures.

When performing 3D analysis of pulmonary vasculature from macro- to micro-structural level, different techniques can be considered. First, optical serial block face imaging (SBFI) is used for macrostructural visualization as it is designed to generate a 3D reconstruction of a sample via automated serial image acquisition during sectioning for histological analysis. Surface imaging of the embedded tissue is captured digitally, allowing the generation of a digital 3D volume in a label-free approach [9, 10]. Structural differences and autofluorescence properties of airways and lung parenchyma allow the visualization and quantification of both airways and aligned vascular components, as well as their structural relationships.

Second, nondestructive 3D imaging includes the use of X-ray radiation sources for microcomputed tomography (micro-CT) to obtain high-resolution 3D structural visualization of the pulmonary vasculature [11, 12]. In spite of the high spatial resolution of such X-ray-based techniques, the small difference in attenuation coefficient (Z) between blood vessels and surrounding tissue makes it challenging to differentiate the vascular system and potential pathological regions [13–17]. Consequently, lung vascular imaging requires the use of high-Z contrast agents. Although significant progress has been achieved in live, in vivo micro-CT imaging of blood vessels in small animals, the presence of respiratory and cardiac motion, as well as the high contrast difference with surrounding bones poses challenges in extracting all the characteristics of the pulmonary microvasculature [8, 18]. *In vivo* micro-CT remains limited in its capability to visualize the microcirculation [19].

Therefore, ex vivo micro-CT on isolated lungs is used for visualization of the distal segments of the lung vasculature. Ex vivo micro-CT benefits from higher spatial resolution by avoiding motion artifacts and interference from surrounding tissues, such as bones. Additionally, the radiation dose is no longer a limiting factor. Multiple commercially available contrast agents have been developed for ex vivo micro-CT and applied for perfusion and imaging of systemic organs in experimental research as they form a vascular cast, providing better contrast [20–23]. Towards lung imaging, perfusion of the pulmonary vasculature is very challenging due to the low-pressure system. An optimal perfusion pressure is crucial to obtain reproducible data as deviations in perfusion can easily lead to over- or under-perfusion of the microcirculation which adversely affects analysis.

To avoid high perfusion pressures that may cause structural modifications, nondestructive optical tomography can be used as an alternative method since it demonstrates potential in imaging the pulmonary microvasculature. As optical imaging relies on the use of small molecule fluorescent dyes or antibody labeling, there is no need to risk over- or under-perfusion of the lung microcirculation. Optical imaging modalities such as optical projection tomography (OPT) allow nondestructive mesoscopic analysis of optically transparent mouse lungs [24–26]. When combined with light sheet fluorescence microscopy (LSFM) [27], this technique enables 3D mesoscopic reconstruction with microscopic resolution, thus allowing visualization of individual fluorescently labeled cells and enabling the study of their spatial relationships [28, 29]. To make tissue optically transparent, several clearing methods have been developed, including hydrophobic (solvent-based) tissue clearing, hydrophilic (aqueous-based) tissue clearing, or hydrogel-based clearing [30–33]. Each of these existing clearing approaches has their pros and limitations [34]. These clearing methods can be compatible with a range of fluorescent labels, whether they be endogenous fluorescent markers, exogenous antibodies, or fluorescent dyes, depending on the chosen method. However, the need for a tailored clearing strategy to match the choice of endogenous fluorescent labels, exogenous antibodies, or fluorescent dyes further amplifies the complexity of available options. The rapid, efficient, and cost-effective labeling of pulmonary vasculature using Evans Blue (EB) as a fluorescent dye enables the visualization of the entire lung blood vasculature [32, 35]. Although EB is able to label large vessels, its capacity to label distal microvessels and capillaries is currently unknown. The exploitation of LSFM for visualization and reconstruction of the complete pulmonary vascular tree up to precapillary pulmonary microvasculature has not been previously attempted. Exploring whether EB is able to label the pulmonary arterial vascular network down to the microscopic level using LSFM may provide valuable insights into pathophysiological processes and pulmonary vascular dynamics. The combination of the EB fluorescent dye and the lung tissue's autofluorescent properties allows the simultaneous visualization of airways and aligned vascular structures using optical imaging, enabling the exploration of their intricate 3D structural relationships.

In this study, we have optimized and implemented various advanced imaging modalities including SBFI, ex vivo micro-CT, and OPT-LSFM, for visualizing the pulmonary vasculature in mouse lungBeyond mere visualization, our objective is to push the boundaries of these modalities, focusing on capturing the intricate details of the lung vasculature from macro- to micro-structural levels.

1 | Methods

1.1 | Animals

All experimental procedures were approved by the Animal Ethics Committee of KU Leuven (P149/2021). Adult mice were used to optimize the procedures and protocols. The animals were housed at the animal facility of KU Leuven in standard individually ventilated cages under a 12 h light/dark schedule. Environmental conditions, such as humidity (50%–70%) and temperature (22 ± 2°C), were controlled. Food and water were supplied ad libitum. Before lung sample preparation and collection, animals were terminally anesthetized by intraperitoneal injection of an overdose of sodium pentobarbital (Dolethal, Vétoquinol SA, France) until the animal exhibited no reflex responses. Unless mentioned otherwise, the trachea was exposed, and a catheter (20 GA, 1.1×30 mm, BD Insyte W) was inserted through tracheotomy. Next, a thoracotomy was performed and the left atrium was cut. Next, a butterfly needle (27 G, 0.4×16 mm, Venoflux Vygon) was inserted through the right ventricular outflow tract towards the pulmonary artery to enable perfusion with 10 mL of heparinized warmed saline infused at a constant perfusion rate of 2 mL/min using a perfusion pump (CMA 400 Syringe Pump). Additionally, the vena porta was cut to prevent venous return. After successful perfusion, when the lungs appeared white and the perfusate did not contain any blood, the lungs were inflated via the trachea with 4% paraformaldehyde (PFA) in PBS at 15 cm H_2O until all lobes were uniformly filled.

1.2 | Serial Block Face Imaging

Upon perfusion and inflation of the murine lungs, the heart-lung complex was collected en bloc and fixed in 4% PFA for 24 h. Following cleaning and separation of the heart and lung, the lung samples were dehydrated in absolute ethanol and embedded in 5% Oil red O (ORO)-colored (Diapath, Italy) paraffin (Paramat Gurr, VWR) to reduce out-of-focus signal diffusion [9]. The samples were processed on a SBFI system, the Kratoscope (Kaer labs, Nantes, France). Briefly, the paraffin block was mounted onto a rotary microtome with a section transfer system (STS). The camera was positioned in front of the surface block, which is sequentially imaged and sectioned. The process is automated and controlled by the software interface. Individual lenses can be mounted on the system to adapt the field of view (FOV) and the pixel size of the acquisition to the size of the processed sample (Table 1). Images of the block were captured using tissue autofluorescence by exciting the sample with 405 nm light and detected above 500 nm. The excitation power and integration time were controlled through the interface. Next, 10 μm thick sections were cut and the collected images of the freshly-cut block face were rendered to generate a 3D volume. Image segmentations of blood vessels and airways were performed manually using the smart brush option in Mimics Innovation Suite 24 (Materialize, Leuven, Belgium) and using the machine learning pixel classification on Imaris software by annotating regions of interest and background signal on a few images. The automated workflow was then applied to the full image stack. 3D rendering and animations were also performed on Imaris.

1.3 | Lung Vascular Perfusion With Radio-Opaque Contrast Agent

Mice were heparinized (LEO Pharma, 5000 I.U./mL) 5 min before being euthanized. Next, the trachea was exposed, and a catheter (20 G, BD Insyte-W, Vialon material, Spain) was inserted and coupled to a ventilator (MiniVent Type 845, Hugo Sachs Elektronik, Germany), ventilating the animals with a tidal volume of 350 μL and 60 breaths per minute during the perfusion procedure. Using a heat lamp, we maintained a constant and physiological body temperature during the procedure. Next, a thoracotomy was performed and the surgical procedures were performed as mentioned above. After successful vascular perfusion, presented by clear perfusate and white lungs, the blood vessels of the lungs were infused with 1 mL warmed Vascupaint mixture of Vascupaint Lime with Diluent in a 4:5 ratio added with 1:20 water-based catalyst until the lungs were completely perfused with vascular contrast agent and decolored. Finally, the ventilation was stopped, and lungs were inflated via the catheter with 4% paraformaldehyde (4% PFA in phosphate-buffered saline (PBS, Acros Organics, Germany) at 15 cm H_2O until all lobes were uniformly inflated. Simultaneously, the lungs were covered with wet paper tissue for at least 1 h to ensure the Vascupaint solidified. Next, the heart and lungs were removed en bloc and stored in 4% PFA for post-fixation for 24 h at 4°C. After fixation, the heart and lungs were separated and stored in PBS with 0.2% sodium azide (Sigma-Aldrich, St. Louis, MO, USA) until micro-CT scanning.

1.4 | Micro-CT Image Acquisition Protocol and Image Reconstruction

The samples with radio-opaque contrast-filled vasculature were placed in a column stage filled with PBS and immobilized (Figure 2C) before being scanned using a high-resolution micro-CT

TABLE 1 | Summary of possible zoom levels on the Kratoscope. Depending on the zoom level of the mounted lens (level 0–level 3), the FOV on the tissue and the pixel size differ according to the data in the table.

Zoom	Field of View (mm)	Pixel size (μm)
0	24.0	23.4
1	11.0	10.7
2	7.0	6.7
3	4.0	3.9

desktop scanner, Skyscan 1272 (Bruker microCT, Kontich, Belgium). The lungs were imaged with a 1 mm aluminum filter at 80 kV, 125 mA, 9.977 μm reconstructed voxel size, 0.4° rotation step, and 10 projections with 1050 ms exposure time were taken at each angle and averaged. Data reconstruction, lung tissue and blood vessel segmentation, and postprocessing were performed with software from the manufacturer (NReconServer64bit, CTAn, Bruker microCT). CTVox (Bruker microCT) and Imaris 10.0.1 (Oxford Instruments, Abingdon, UK) software were used for volume rendering and 3D visualization.

1.5 | Micro-CT Image Analysis

The micro-CT stacked images were imported into FIJI software equipped with the 3D ImageJ suite and MorpholibJ plug-ins [36–38], and analyzed with a custom-written ImageJ macro script. To segment the blood vessels, a threshold was applied to the image stacks and filled using the "3D fill holes" tool from the 3D suite, ensuring the blood vessels were completely filled. At this point, we had the 3D structure of the blood vasculature digitized.

In the next step, we segmented the lung mask to obtain the tissue volume as a normalizing parameter and the filled blood vessels were downscaled by a factor of 10 in 3D. A 3D Gaussian blur with a sigma value of 5 was applied to smooth and close any remaining gaps in the structure. Subsequently, the resulting void regions were filled using the fill holes function and the lung mask was rescaled to match the original image size. This yielded the 3D volume of the lung tissue.

Next, we extracted the blood vessel properties, including volume, surface area, and local thickness, as well as the lung volume used for normalization which were determined using the Analyse Regions 3D function provided by MorpholibJ [37]. The blood vessel's local thickness was calculated using the Analyse/Local Thickness tool. To assess the local separation, the local thickness function was applied to an image generated by subtracting the filled blood vessels from the lung mask. Additionally, the filled blood vessels were skeletonized in 3D and analyzed without pruning to calculate the number of branches, junctions, and branch length. The Strahler analysis was performed through an iterative loop and end-point elimination until reaching a single pixel. Data were analysed using Prism 9.5.0 (GraphPad). Local thickness, separation, and branch length were shown as frequency distributions. Blood vessel volume, surface, branch, and junction number parameters were normalized to the lung volume.

1.6 | Sample Preparations for Optical Clearing and Imaging

Adult mice were terminally anesthetized, and the lungs were perfused and inflated, as mentioned earlier. The lungs were collected en bloc and fixed in 4% PFA for 24 h. The heart and lung lobes were separated and washed in PBS. Next, the left lung was incubated in a PBS-Tween 0.01% solution with 10% DMSO and 0.5% EB dye (Sigma-Aldrich, St. Louis, MO, USA) for passive staining overnight. The lung was washed three times in PBS for 2 h to rinse excess EB. Then, the samples were embedded in 1% low melting point agarose (Sigma-Aldrich, St. Louis, MO, USA) for better handling and scanning. The embedded tissues were dehydrated in graded methanol/PBS series (30%, 50%, 70%, 90%, 100%, 100%) for at least 2 h each step at room temperature in the dark under constant gentle shaking. Finally, the tissues were transferred to a benzyl alcohol-benzyl benzoate (BABB) clearing solution consisting of one-part benzyl alcohol (Sigma-Aldrich, St. Louis, MO, USA) and two parts benzyl benzoate (BABB, Sigma-Aldrich, St. Louis, MO, USA) for at least 24 h at room temperature and all samples were stored in the dark untill further use.

1.7 | Lung Imaging Using Optical Projection Tomography and Light Sheet Fluorescence Microscopy

The lung lobes were imaged in BABB using; (I) a custom-built optical projection tomography (OPT) machine; (II) an LCS-SPIM (Luxendo, Bruker, USA) and (III) a MuViSPIM (Luxendo, Bruker, USA). Using the custom-built OPT, lung airway structures were visualized by autofluorescence (using a 470/40 nm excitation filter and a 525/50 nm emission filter) and the lung vasculature capturing the EB fluorescent dye using a cy5 filter (620/60 nm excitation filter and a 700/75 nm emission filter). 400 images with an image rotation step of 0.9° were captured per channel and used for reconstruction. We optimized the excitation power of each channel independently for maximal S/N (signal-to-noise-ratio) and to avoid saturation of differently sized structures.

Light sheet microscopic imaging was performed using the LCS-SPIM (Luxendo, Bruker) equipped with one Olympus 4×0.28 NA air/dry detection lens and an additional magnification changer, resulting in a total magnification ranging between 2.2× and 8.8×. Image stacks covering the full lung lobe were taken at 2.2× magnification ($x = 2.96\,\mu m$, $y = 2.96\,\mu m$, and $z = 5.00\,\mu m$ pixel size) and stitched using the Luxendo commercial software. Local stacks of specific regions within the lung were captured at 8.8× magnification ($x = 0.74\,\mu m$, $y = 0.74\,\mu m$, and $z = 5.00\,\mu m$ pixel size). A laser with a 488 nm wavelength was used for the excitation of autofluorescence, and a 642 nm laser was used to excite the EB fluorescent dye.

For an even more detailed view of the lung parenchyma, we used the MuVi SPIM CS (Luxendo, Bruker) equipped with a Nikon 10×0.5NA dipping lens resulting in a maximum magnification of 20× ($x = 0.33\,\mu m$, $y = 0.33\,\mu m$, and $z = 2.00\,\mu m$ pixel size) and the 488 nm laser and 594 nm laser for excitation of autofluorescence and EB fluorescent dye, respectively. The software provided by the manufacturer (Bruker) and ImageJ were used for visualization.

2 | Results

2.1 | SBFI Captures the Vascular Macrostructures in Combination With Lung Airways

We applied SBFI on a perfused mouse left lung to investigate its capacity to visualize, reconstruct and quantify the pulmonary

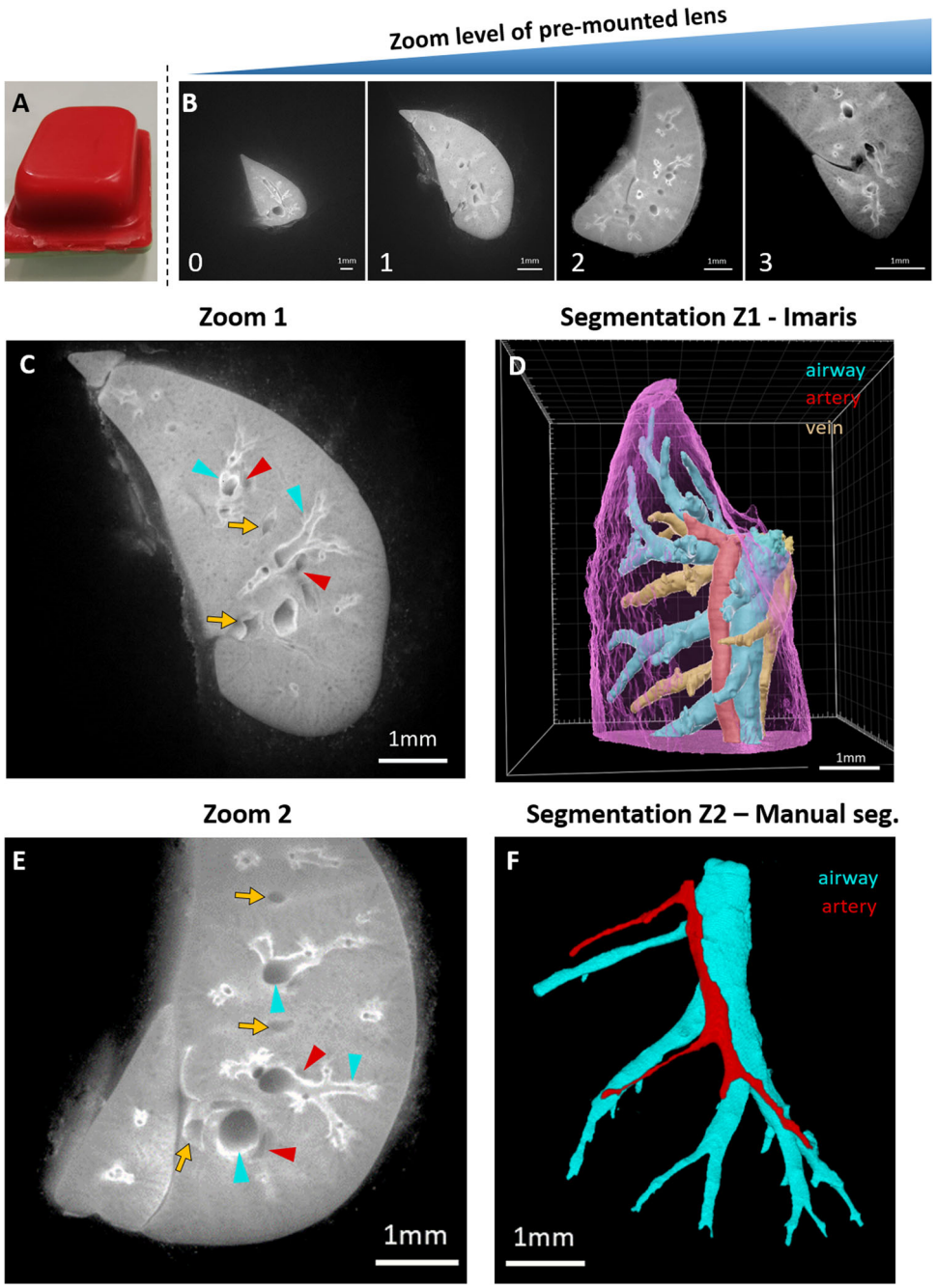

FIGURE 1 | Overview of the Kratoscope workflow and 3D segmentation of arteries and airways. (A) Samples of interest embedded in Oil red O-colored paraffin. (B) Representative images of the different zoom levels, scale bars 1 mm. See Video S1 also. (C) One block face image taken at zoom 1 indicating airways (cyan arrowheads), arteries (red arrowheads) and veins (yellow arrows). (D) semi-automated 3D segmented view of Zoom 1 using Imaris software presenting airways, lung arteries and veins. (E) One block face image taken at zoom 2 indicating airways (cyan arrowheads), arteries (red arrowheads) and veins (yellow arrows). (F) Manual 3D segmentation of zoom 2 presenting airways aligned by the lung arteries (See Video S2 also).

vasculature. At zoom 0 and zoom 1, we were able to section throughout a full mouse lung lobe with a pixel size of 23.4 μm (zoom 0) and 10.7 μm (zoom 1) (Figure 1B,C, Video S1 and S2). Depending on the preferred orientation (frontal, sagittal, or transversal plane) for the collected lung slices, the zoom could be optimized. Higher zoom levels, with an in-plane pixel size of 6.7 μm (zoom 2) and 3.9 μm (zoom 3), were performed on the middle right lung lobe to fit the smaller FOV (Figure 1B,C, Video S1) and allowed a more detailed view of the 3D branching of the pulmonary vasculature and airway tree. Based on the autofluorescent signal of lung airways, this label-free approach allowed us to distinguish between airway and blood vascular structures. Notably, the use of the Kratoscope, as an example of the SBFI technique, enabled the simultaneous analysis of both the macrovascular network and large airways, allowing us to study the intricate interplay between airways and vasculature (Figure 1C,E). Arteries and veins could be distinguished based on the location, that is, where arteries align with the airways. By digitally acquiring each section, we next conducted a 3D volume segmentation of the mouse lung vasculature in parallel

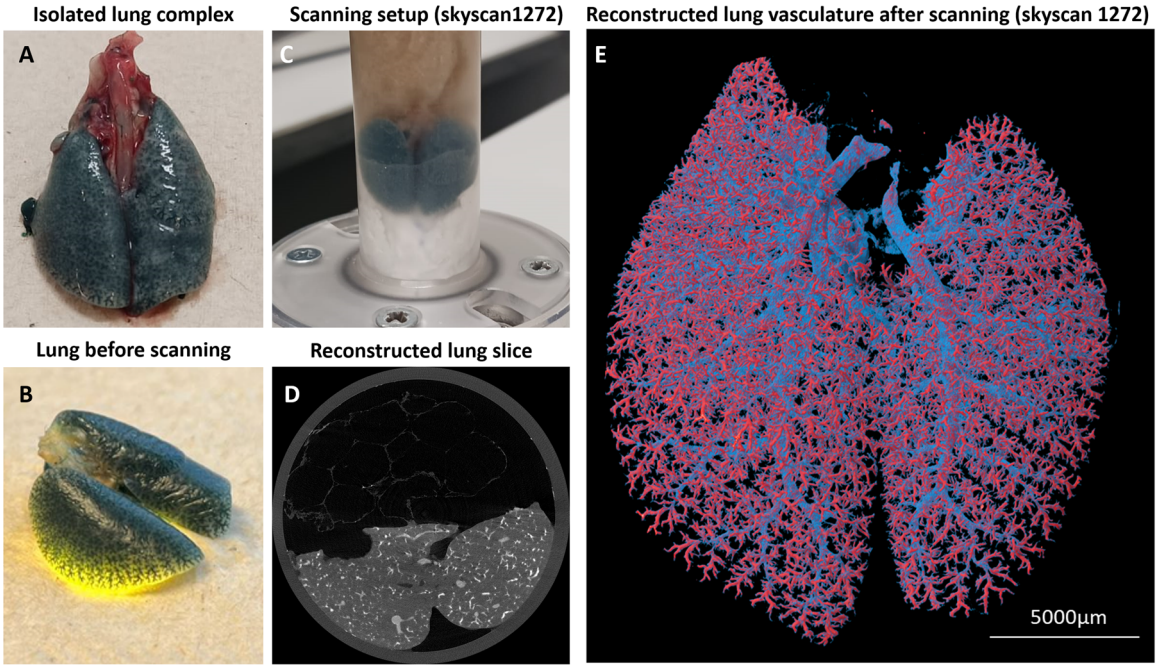

FIGURE 2 | Overview of micro-CT setup and visualization of the arterial bed. (A) heart-lung complex of Vascupaint-lime perfused lungs demonstrating a uniform filling of the lungs with contrast agent. (B) Isolated lungs presenting visible contrast-filled blood vessels reaching distal lung regions. (C) sample mounting before scanning. (D) Tomographic image showing perfused blood vessels in white pixels. (E) 3D volume rendering of a lung complex showing uniform vascular perfusion with a reconstructed voxel size of 4.7 µm and colors presenting density variations (See Video S3).

with the airways in a manual and semi-automated manner (Figure 1D,F, Video S2). The 3D segmentation showed that using the Kratoscope, we were able to capture the macrovasculature and large airways up to the third and fourth generation with the label-free approach, which is insufficient for the observation of microvasculature and small airway structures. However, visual assessment of these regions is possible.

2.2 | Micro-CT Allows Microstructural Visualization and Quantification of the Complete Lung Complex

To gain deeper insight into the lung microvascular structures, we optimized an ex-vivo micro-CT approach to visualize the precapillary arteries. To visualize the blood vessels using micro-CT, we used a radio-opaque filling agent as a contrast perfusion agent (Figure 2A,B). We demonstrated an effective perfusion resulting in the filling of the complete pulmonary vascular tree. We observed a green colorization of the full lung tissue (Figure 2A) with vessel-like structures in the lung parenchyma (Figure 2B). The full mouse lung (including left and right lungs) was scanned using micro-CT with a reconstructed isotropic voxel size of 4.7 µm (Figure 2C,D). After micro-CT reconstruction, we clearly observed the main pulmonary arteries branching to arteries and distal arterioles (Figure 2E, Video S3).

Our in-house automated 3D analysis demonstrated the feasibility of quantifying the relative vascular volume based on the generated lung tissue mask (Figure 3A). Besides the tissue mask, we extracted local thickness (Figure 3B) and local separation (Figure 3C), which provided an estimate of the distribution of the perfused vessels and vessel diameters throughout the different generations. The skeleton of the blood vessels (Figure 3D,E) allowed the extraction of distributions on vessel length, vessel diameter and vessel separation (Figure 3F). Additionally, the number of branches, junctionsand number of generations was obtained from the analysis (data not shown). In our representative example of the Vascupaint-perfused lung, the analysis revealed a vascular volume fraction of 10% with 17 generations, corresponding to the maximum number of generations observed in mice. This implies that this perfusion technique is able to image and quantify the precapillary arteries and microvasculature. With the combined information on the number of generations, vessel volumes, branch length distributions, vessel diameter separation, and vessel separation distribution (Figure 3F) it is feasible to differentiate between proximal and distal vascular pathologies.

2.3 | Nondestructive Optical Projection Tomography and Light Sheet Fluorescence Microscopy Visualizes the Vasculature Down to Capillary Level

To overcome the need for vascular filling with a radio-opaque contrast agent and thereby avoiding the potential to over- or underperfuse the vasculature, we implemented nondestructive lung optical imaging as a technique to visualize the 3D pulmonary vasculature down to the precapillary level. The fluorescent EB labeling is compatible with our BABB organic solvent clearing agent (Figure 4A). The autofluorescent properties of the lung were used to visualize the large airway structures in parallel with the macrovascular structures. The fluorescent signal of EB-labeled vessels was captured in 3D at the level of the full left lobe (Figure 4A). While the arteries clearly align with the airways, the veins are not surrounded by large airways and present a lower EB intensity together

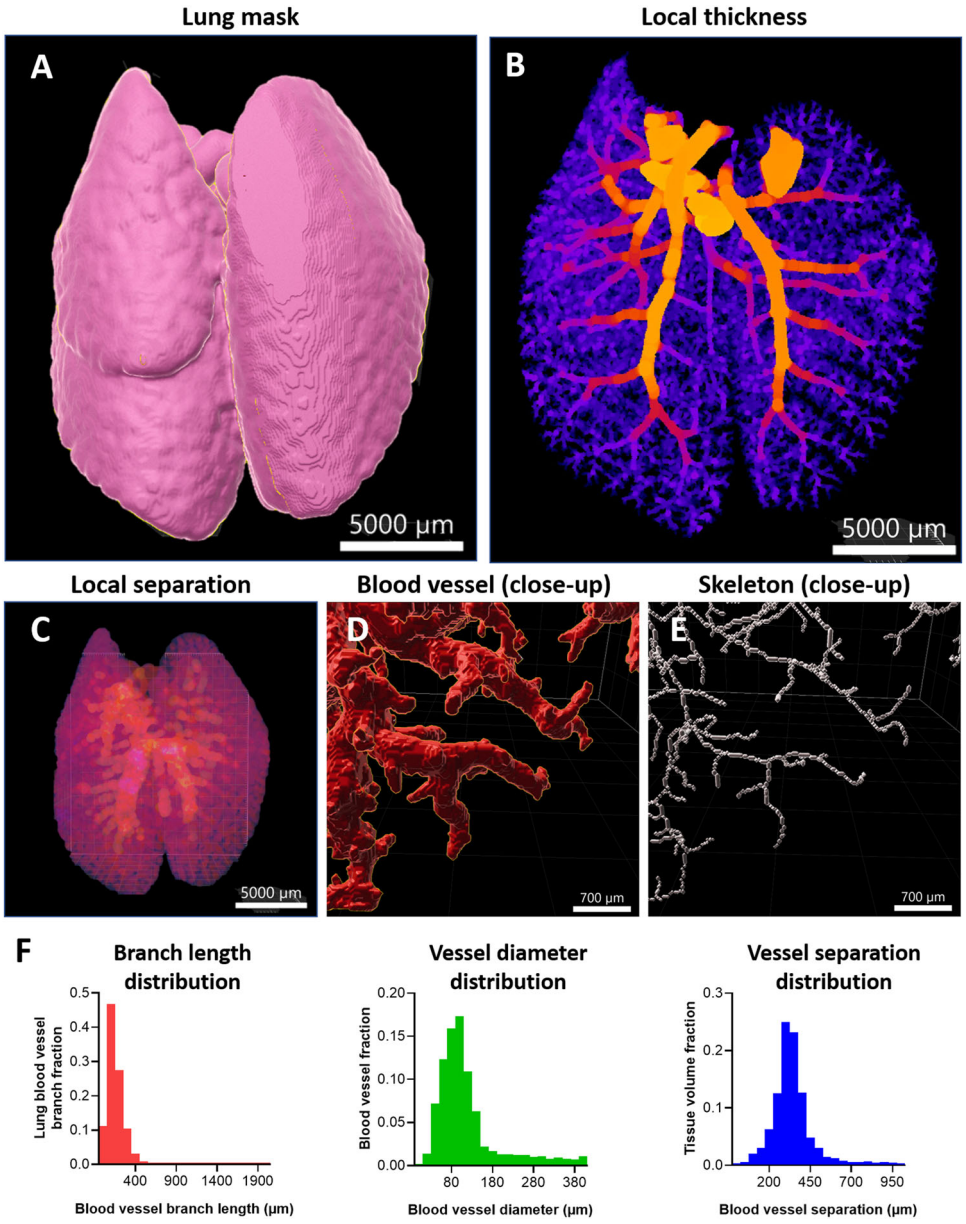

FIGURE 3 | Arterial analysis of contrast-perfused mouse lung for micro-CT. (A) 3D view of the tissue mask of the perfused mouse lung, scale: 5000 µm. (B) 3D visualization of the representative local diameter and (C) local separation of the lung vasculature, scale: 5000 µm. (D) Close-up of the distal regions of the lung vasculature, scale: 700 µm (E) Visualization of the extracted skeleton of region shown in D), scale: 700 µm. (F) Analysis of micro-CT perfused lungs with quantification of branch length distribution, vessel thickness distribution, and vessel separation distribution.

with some autofluorescent signal in the large veins. The combination of the structural orientation and differences in staining due to composition of the vessel wall allows the differentiation between arteries and veins (Figure 4A, Video S4).

The same sample was scanned using the LCS-SPIM to investigate if we were able to visualize the microstructures of the pulmonary vasculature. Stitching of different LCS-SPIM stacks (at 2.2× magnification) showed a full view of the mouse left lung lobe at a smaller voxel size than the OPT data, enhancing the visualization of the smaller vascular branching pattern (compare Figure 4B to 4A, Video S5). Inspection with increased magnification (8.8x) using the LCS-SPIM clearly showed the arteries lining along the airways up to the level of terminal bronchioles, allowing the visualization of the pulmonary vasculature up to the arteriolar level (Figure 4C, Video S5).

In addition, the use of MuViSPIM with 20× magnification enabled visualization at the microstructural level. The MuViSPIM effectively revealed EB-labeled precapillary vessels within a defined lung region, allowing for the precise tracing of both vascular and airway structures in 3D (Figure 4D, Video S6).

3 | Discussion

In this study, we optimized and implemented multiple state-of-the-art techniques for 3D lung vascular imaging, overcoming the limitations inherent to conventional 2D histological methods. Previous

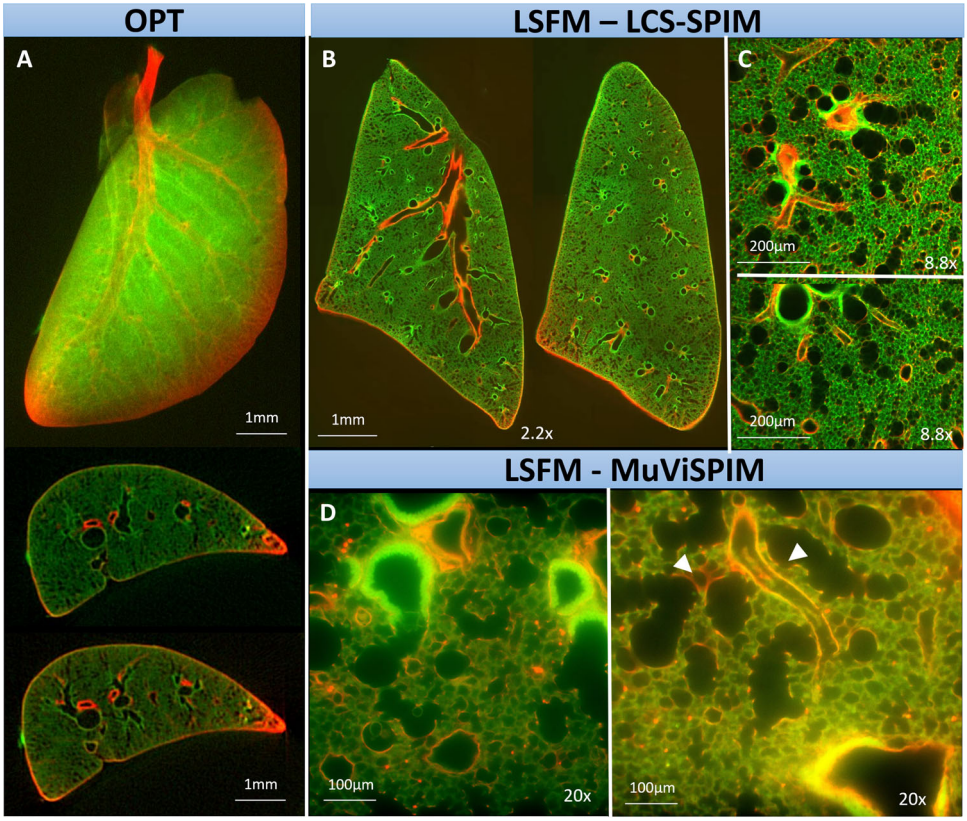

FIGURE 4 | Visualization of the vasculature with OPT and LSFM. (A) OPT projection of a mouse lung (top) cleared with BABB and reconstructed tomographic slices (middle and bottom) showing 3D airway structures (470/40 nm excitation filter, 535/50 nm emission filter) in green and blood vessels (EB fluorescent dye, 620/60 nm excitation filter, 700/75 nm emission filter) in red. Airways (cyan arrowhead), arteries (red arrowhead) and veins (yellow arrows). See Video S4. (B) LCS-SPIM slices from stitched stacks covering the full left lung lobe at 2.2× magnification. See Video S5. (C) representative images at 8.8× magnification. (D) MuViSPIM images at 20× magnification, highlighting EB stained microvessels (red arrowhead) at precapillary level aligning terminal bronchioles and alveolar sacs (cyan arrowhead) (See Video S6 also).

research has often overlooked the intricate complexities of lung vasculature due to gaps in methodological approaches. To bridge this gap, we present our expertize in visualizing the pulmonary vasculature in 3D from macro- to micro-structural scales and quantification using SBFI, micro-CT, optical tomography, and light sheet fluorescence microscopy.

SBFI systems offer a rapid, cost-effective, label-free method for 3D macrostructural imaging of entire mouse lungs alongside histological analysis. Although SBFI primarily captures macrostructures and large vessels, arteriolar levels can be visualized based on the chosen field of view (FOV) and zoom level. Optimal zoom selection is crucial to avoid post-processing complications and incomplete 3D visualization. Post-processing of SBFI-generated images is uncomplicated. The data set, up to several gigabytes, can be segmented and visualized using free software like Ilastik, ITK-SNAP, Icy, Dragonfly, or ImageJ, and in combination with semi-automated segmentation software like Imaris, yielding results within 3 days. Preclinical research on diseases like arterial banding, pulmonary embolism, or lung pathologies affecting large airways, benefits from simultaneous visualization of both airway and arterial structures.

While SBFI does not inherently provide vascular-specific imaging, resulting in uncertainty about whether the vessels are arteries or veins, the incorporation of fluorescent agents can significantly enhance the specificity and quality of the imaging. Additionally, vascular filling with gelatin or silicone-based contrast agents can also improve vascular visualization and may act as a complementary tool in cases where arterial collapse due to lung inflation is observed. These enhancements in sample preparation can be used to better distinguish between arteries and veins, thereby improving the scientific value of the reconstructed 3D images.

Using ex vivo micro-CT, we are able to visualize the arterial circulation and even (pre)capillary structures with micrometer resolution (down to 3 µm isotropic voxel size), which is of interest when focusing on vasculopathies characterized by microvascular rarefaction or pruning. Using our custom-built ImageJ macro script, we are able to extract the distribution of branch length and vessel diameter as well as the number of arteries per generation to analyze the spatial distribution, and differentiate between proximally and distally affected regions. This method is particularly promising in models featuring microvascular rarefaction and pruning, emphasizing the importance of visualizing and quantifying the intricate microcirculatory network. The algorithm is generic and can be applied to various animal models and organs. The advantage of visualizing the entire lung complex can be particularly relevant in animal models involving arterial banding or single lung transplantation as differences between left and right can be easily observed by differences in local separation [39, 40]. However, a high-level processing computer is required for the post-processing and analysis as

TABLE 2 | Summary of key features of SBFI, micro-CT, and nondestructive optical projection tomography and light sheet fluorescence microscopy. The performance of each aspect is depicted using a color-code; good performance in green, moderated in yellow and weak in red.

	SBFI	Micro-CT	OPT/LSFM
Time (collection to analysis)	3 days	2 days	14 days
Resolution voxel size	24 –> 7 μm	< 10 μm	down to < 1 μm
Size data set	1–2 Gb	10–20 Gb	200–500 Gb
Sample size	Full lung complex (Z0)	Full lung complex	One lung lobe
Reversible	No	No	Yes
Labeling	Label-free	Perfusion with CA	i.v./passive staining
Visualization	macrostructure	microstructure	Macro- and microstructure
Segmentation	Semi-automated	Automated	Semi-automated
Quantification	Yes	Yes	Semi-quantitative
Zoom possible	Yes, but destructive	Yes, FOV-dependent	Yes
Combination with histology?	Yes	Yes	Yes
Correlation with Histology	Yes	No	No

the datasets are in the range of 20–30 gigabytes for a full mouse scan down to a resolution of 5 μm.

Perfusing the pulmonary circulation with highly viscous contrast agents is challenging since improper adjustments can easily lead to under- or over-perfusion, potentially disrupting capillary beds and alveolar spaces [16, 41, 42]. Especially when advancing to disease models, for example in the context of pulmonary hypertension, individualized perfusion pressures are essential to accurately replicate pathological changes. Maintaining a matching right ventricular systolic pressure is crucial for consistent comparison of 3D vascular trees across animals. Individualized perfusion pressures are necessary for obtaining comparable quality radiographs in normal and hypoxic rats, with the latter requiring higher pressures due to vasoconstriction and increased vascular resistance [41]. Measuring the right ventricular systolic pressure in mice is surgically challenging and therefore, the use of a steady-state perfusion pump is important for a successful and uniform perfusion. Other critical steps for complete vascular perfusion include: (I) initial flushing with warmed, heparinized saline to prevent vasoconstriction and clotting, avoiding underestimation of the pulmonary vascular volume [16]. (II) Ventilating mice for optimal microvascular filling during lung inflation.

To avoid the need to apply high perfusion pressures, we adopted a nondestructive optical approach. OPT, in combination with EB fluorescent labeling, can capture the pulmonary vasculature at the whole-lung level without inducing adverse hemodynamic changes. In conjunction with LSFM techniques, our findings underscore the capacity to nondestructively label and visualize the microvasculature of optically cleared mouse lungs down to the precapillary level [25, 26].

In this study, we optically labeled the blood vasculature by incubating the lung in an EB solution for 24 h post-fixation. Alternatively, EB staining can be achieved through (I) intravenous injection up to 2 days before sacrifice [39] or (II) intracardial injection with a 5-min circulation [32], demonstrating in vivo vascular staining at hemodynamic pressures for complete labeling. EB offers cost savings compared to antibody labeling, quick staining, and resistance to photobleaching. Additional staining with lectins, wheat germ agglutinin (WGA), or endothelial-specific antibodies can enhance the microvascular signal [35, 40]. EB labeling also allows for simultaneous antibody staining, enabling multiplexing for visualizing various structures (airway, vasculature, or lymphatics) and specific cells [43, 44]. The implementation of vascular-specific antibodies may be necessary when advancing this technique to disease models as disruption of endothelial barriers and leaky vessels may cause non-specific EB staining. The advantage of using antibodies is that they have a smaller emission spectrum, meaning that it is easier to implement multiple stainings.

In our study, we employed the BABB clearing method, which proved to be both robust and rapid. A limitation of the clearing process is that shrinkage of the sample may occur using organic solvents-typically a linear shrinkage of the sample by 10% can occur. The dehydration and clearing process are the most time-consuming steps [34]. The duration from sample collection to imaging acquisition may extend up to 2 weeks, depending on the selected staining procedure. Operating on a whole organ level with micrometer resolution yields datasets in the range of several hundred of gigabytes. These considerable data volumes can pose computational challenges for 3D rendering or quantification.

The feasibility to combine OPT for lower-resolution imaging of the entire lungs with LSFM to examine subregions at high resolution is unique, providing a comprehensive overview of the entire lung while enabling detailed zooming into specific precapillary and alveolar regions.

Finally, it is crucial to underscore the versatility and compatibility of these techniques for advancing our understanding of the pulmonary vasculature (Table 2). The selection of a specific technique must align with the intended application and

available resources. When employing micro-CT of contrast-perfused lungs, integration of optical clearing can prove advantageous by minimizing background noise [45, 46]. Additionally, the Kratoscope, relying on fluorescent signals, can be effectively utilized alongside EB-perfused lungs or lungs perfused with agents for micro-CT, facilitating a cleared distinction between vasculature and airways. This approach requires an additional step in the workflow compared to a label-free sample preparation but can be used to enhance the internal contrast of structures of interest and improve detection resolution. This adaptability not only enhances the landscape of pulmonary research but also grants researchers the flexibility to choose the most suitable approach based on the unique requirements of their investigation. Our study emphasizes the importance of investigating the pulmonary vasculature in both healthy and diseased states by employing these cutting-edge techniques, and provides 3D visualization techniques for enhanced knowledge and expedited bench-to-bed translation.

Author Contributions

B.T. and G.V.V. conceived and designed research. B.T., N.F.M., A.K., M.C.L., N.G., P.D.V., and M.O. performed experiments. B.T., N.F.M., N.P., N.G., V.G., and B.L. analyzed data. B.T., N.F.M., A.K., N.P., M.C.L., N.G., P.D.V., P.D., S.B., B.L., J.S., and G.V.V. interpreted results of experiments. B.T., N.P., P.D.V., V.G., and B.L. prepared figures. B.T., and N.F.M. drafted manuscript. A.K., N.P., M.C.L., N.G., P.D.V., P.D., V.G., M.O., S.M., B.L., J.S., and G.V.V. edited and revised manuscript. B.T., N.F.M., A.K., N.P., M.C.L., N.G., P.D.V., P.D., V.G., M.O., S.M., B.L., J.S., and G.V.V. approved the final version of the manuscript.

Acknowledgments

All imaging using the micro-CT was performed in collaboration with the KU Leuven XCT core facilty and the authors would like to thank Lieve Verlinden for her assistance with acquisition. Optical imaging was performed in collaboration with VIB–Bioimaging Core Leuven and the the Mesoscopic Imaging Facility at EMBL, Barcelona. This project was funded by departmental grants received in 2022 and 2023 by the Department of Imaging and Pathology, KU Leuven. A FWO fellowship "short stay abroad" (FWO–K222922N) and Christian Boulin fellowship (EMBL) were received by B.T.

Ethics Statement

The Animal Ethics Committee of KU Leuven approved all experimental procedures, ECD number P149/2021.

Conflicts of Interest

Image acquisition and data collection at the Kratoscope were performed at Kaer Labs company, Nantes, France. P.D.V. and P.D. are employees of the company Kaer Labs.

References

1. B. Tielemans, K. Dekoster, S. E. Verleden, et al., "From Mouse to Man and Back: Closing the Correlation Gap Between Imaging and Histopathology for Lung Diseases," *Diagnostics* 10, no. 9 (2020): 636.

2. A. Huertas, C. Guignabert, J. A. Barberà, et al., "Pulmonary Vascular Endothelium: The Orchestra Conductor in Respiratory Diseases: Highlights From Basic Research to Therapy," *European Respiratory Journal* 51, no. 4 (2018): 1700745.

3. J. May, J. A. Mitchell, and R. G. Jenkins, "Beyond Epithelial Damage: Vascular and Endothelial Contributions to Idiopathic Pulmonary Fibrosis," *Journal of Clinical Investigation* 133, no. 18 (2023): e172058.

4. I. Blanco, L. Piccari, and J. A. Barberà, "Pulmonary Vasculature in COPD: The Silent Component," *Respirology* 21, no. 6 (2016): 984–994.

5. M. Humbert, C. Guignabert, S. Bonnet, et al., "Pathology and Pathobiology of Pulmonary Hypertension: State of the Art and Research Perspectives," *European Respiratory Journal* 53, no. 1 (2019): 1801887.

6. C. C. Hsia, D. M. Hyde, M. Ochs, and E. R. Weibel, "How to Measure Lung Structure—What For? On the "Standards for the Quantitative Assessment of Lung Structure," *Respiratory Physiology & Neurobiology* 171, no. 2 (2010): 72–74.

7. C. C. W. Hsia, D. M. Hyde, M. Ochs, and E. R. Weibel, "An Official Research Policy Statement of the American Thoracic Society/European Respiratory Society: Standards for Quantitative Assessment of Lung Structure," *American Journal of Respiratory and Critical Care Medicine* 181, no. 4 (2010): 394–418.

8. D. M. Vasilescu, L. Knudsen, M. Ochs, E. R. Weibel, and E. A. Hoffman, "Optimized Murine Lung Preparation for Detailed Structural Evaluation via Micro-Computed Tomography," *Journal of Applied Physiology* 112, no. 1 (2012): 159–166.

9. M. Malloci, P. Villemagne, de, P. Dorval, et al., "Label-Free Imaging of Large Samples: 3D Rendering and Morphological Analysis Within Histological Workflows Using Serial Block Face Imaging," *Bioengineering* (2022), https://doi.org/10.1101/2022.05.03.488912.

10. N. Ishii, Y. Tajika, T. Murakami, et al., "Correlative Microscopy and Block-Face Imaging (Combi) Method for Both Paraffin-Embedded and Frozen Specimens," *Scientific Reports* 11, no. 1 (2021): 13108.

11. S. T. Gammon, N. Foje, E. M. Brewer, et al., "Preclinical Anatomical, Molecular, and Functional Imaging of the Lung With Multiple Modalities," *American Journal of Physiology-Lung Cellular and Molecular Physiology* 306, no. 10 (2014): L897–L914.

12. S. Sawall, J. Beckendorf, C. Amato, et al., "Coronary Micro-Computed Tomography Angiography in Mice," *Scientific Reports* 10, no. 1 (2020): 16866.

13. J. L. Cercos-Pita, L. Fardin, H. Leclerc, et al., "Lung Tissue Biomechanics Imaged With Synchrotron Phase Contrast Microtomography in Live Rats," *Scientific Reports* 12, no. 1 (2022): 5056.

14. L. L. Hsu and D. M. Schimel, "Computed Tomography Imaging of Lungs in Mouse Models of Human Disease: Advancing the Computing Interfaces With Physiology." In *Proceedings 17th IEEE Symposium on Computer-Based Medical Systems [Internet]* (Bethesda, MD, USA: IEEE Comput. Soc, 2004), 385–390, http://ieeexplore.ieee.org/document/1311744/.

15. L. Seldeslachts, C. Cawthorne, S. F. Kaptein, et al., "Use of Micro-Computed Tomography to Visualize and Quantify COVID-19 Efficiency in Free-Breathing Hamsters." In *Vaccine Design [Internet]*, ed. S. Thomas (New York, NY: Springer US, 2022), 177–192. (Methods in Molecular Biology; vol. 2410), https://doi.org/10.1007/978-1-0716-1884-4_8.

16. Y. Deng, K. J. Rowe, K. R. Chaudhary, A. Yang, S. H. J. Mei, and D. J. Stewart, "Optimizing Imaging of the Rat Pulmonary Microvasculature by Micro-Computed Tomography," *Pulmonary Circulation* 9, no. 4 (2019): 1–9.

17. S. X. Vasquez, F. Gao, F. Su, et al., "Optimization of MicroCT Imaging and Blood Vessel Diameter Quantitation of Preclinical Specimen Vasculature With Radiopaque Polymer Injection Medium," *PLoS ONE* 6 (2011): e19099.

18. D. M. Vasilescu, C. Klinge, L. Knudsen, et al., "Stereological Assessment of Mouse Lung Parenchyma via Nondestructive, Multiscale Micro-CT Imaging Validated by Light Microscopic Histology," *Journal of Applied Physiology* 114, no. 6 (2013): 716–724.

19. M. Brehm, S. Sawall, J. Maier, S. Sauppe, and M. Kachelrieß, "Cardiorespiratory Motion-Compensated Micro-CT Image Reconstruction Using an Artifact Model-Based Motion Estimation," *Medical Physics* 42, no. 4 (2015): 1948–1958.

20. S. M. Jorgensen, O. Demirkaya, and E. L. Ritman, "Three-Dimensional Imaging of Vasculature and Parenchyma in Intact Rodent Organs With X-Ray Micro-CT," *American Journal of Physiology-Heart and Circulatory Physiology* 275, no. 3 (1998): H1103–H1114.

21. T. Krucker, A. Lang, and E. P. Meyer, "New Polyurethane-Based Material for Vascular Corrosion Casting With Improved Physical and Imaging Characteristics," *Microscopy Research and Technique* 69 (2006): 138–147.

22. L. Schaad, R. Hlushchuk, S. Barré, et al., "Correlative Imaging of the Murine Hind Limb Vasculature and Muscle Tissue by MicroCT and Light Microscopy," *Scientific Reports* 7, no. 1 (2017): 41842.

23. R. Hlushchuk, C. Zubler, S. Barré, et al., "Cutting-Edge Microangio-CT: New Dimensions in Vascular Imaging and Kidney Morphometry," *American Journal of Physiology-Renal Physiology* 314, no. 3 (2018): F493–F499.

24. S. Munck, C. Cawthorne, A. Escamilla-Ayala, et al., "Challenges and Advances in Optical 3D Mesoscale Imaging," *Journal of Microscopy* 286, no. 3 (2022): 201–219.

25. T. Alanentalo, A. Asayesh, H. Morrison, et al., "Tomographic Molecular Imaging and 3D Quantification Within Adult Mouse Organs," *Nature Methods* 4, no. 1 (2007): 31–33.

26. J. Sharpe, U. Ahlgren, P. Perry, et al., "Optical Projection Tomography as a Tool for 3D Microscopy and Gene Expression Studies," *Science* 296, no. 5567 (2002): 541–545.

27. J. Huisken, J. Swoger, F. Del Bene, J. Wittbrodt, and E. H. K. Stelzer, "Optical Sectioning Deep Inside Live Embryos by Selective Plane Illumination Microscopy," *Science* 305, no. 5686 (2004): 1007–1009.

28. R. Tomer, L. Ye, B. Hsueh, and K. Deisseroth, "Advanced Clarity for Rapid and High-Resolution Imaging of Intact Tissues," *Nature Protocols* 9, no. 7 (2014): 1682–1697.

29. B. Yang, J. B. Treweek, R. P. Kulkarni, et al., "Single-Cell Phenotyping Within Transparent Intact Tissue Through Whole-Body Clearing," *Cell* 158, no. 4 (2014): 945–958.

30. K. Tainaka, A. Kuno, S. I. Kubota, T. Murakami, and H. R. Ueda, "Chemical Principles in Tissue Clearing and Staining Protocols for Whole-Body Cell Profiling," *Annual Review of Cell and Developmental Biology* 32, no. 1 (2016): 713–741.

31. E. A. Susaki and H. R. Ueda, "Whole-Body and Whole-Organ Clearing and Imaging Techniques With Single-Cell Resolution: Toward Organism-Level Systems Biology in Mammals," *Cell Chemical Biology* 23, no. 1 (2016): 137–157.

32. S. E. Honeycutt and L. L. O'Brien, "Injection of Evans Blue Dye to Fluorescently Label and Image Intact Vasculature," *Biotechniques* 70, no. 3 (2021): 181–185.

33. E. A. Susaki, K. Tainaka, D. Perrin, H. Yukinaga, A. Kuno, and H. R. Ueda, "Advanced Cubic Protocols for Whole-Brain and Whole-Body Clearing and Imaging," *Nature Protocols* 10, no. 11 (2015): 1709–1727.

34. H. Kolesová, V. Olejníčková, A. Kvasilová, M. Gregorovičová, and D. Sedmera, "Tissue Clearing and Imaging Methods for Cardiovascular Development," *iScience* 24, no. 4 (2021): 102387.

35. M. I. Todorov, J. C. Paetzold, O. Schoppe, et al., "Machine Learning Analysis of Whole Mouse Brain Vasculature," *Nature Methods* 17, no. 4 (2020): 442–449.

36. J. Schindelin, I. Arganda-Carreras, E. Frise, et al., "Fiji: An Open-Source Platform for Biological-Image Analysis," *Nature Methods* 9, no. 7 (2012): 676–682.

37. D. Legland, I. Arganda-Carreras, and P. Andrey, "MorphoLibJ: Integrated Library and Plugins for Mathematical Morphology With ImageJ," *Bioinformatics* 32, no. 22 (2016): 3532–3534.

38. J. Ollion, J. Cochennec, F. Loll, C. Escudé, and T. Boudier, "Tango: A Generic Tool for High-Throughput 3D Image Analysis for Studying Nuclear Organization," *Bioinformatics* 29, no. 14 (2013): 1840–1841.

39. R. T. Robertson, S. T. Levine, S. M. Haynes, et al., "Use of Labeled Tomato Lectin for Imaging Vasculature Structures," *Histochemistry and Cell Biology* 143, no. 2 (2015): 225–234.

40. R. Battistella, M. Kritsilis, H. Matuskova, et al., "Not all Lectins Are Equally Suitable for Labeling Rodent Vasculature," *International Journal of Molecular Sciences* 22, no. 21 (2021): 11554.

41. M. Finlay, G. R. Barer, and A. J. Suggett, "Quantitative Changes in the Rat Pulmonary Vasculature in Chronic Hypoxia - Relation to Haemodynamic Changes," *Quarterly Journal of Experimental Physiology* 71, no. 2 (1986): 151–163.

42. R. C. Molthen, K. L. Karau, and C. A. Dawson, "Quantitative Models of the Rat Pulmonary Arterial Tree Morphometry Applied to Hypoxia-Induced Arterial Remodeling," *Journal of Applied Physiology* 97, no. 6 (2004): 2372–2384.

43. M. Frétaud, D. Descamps, D. Laubreton, et al., "New Look at RSV Infection: Tissue Clearing and 3D Imaging of the Entire Mouse Lung at Cellular Resolution," *Viruses* 13, no. 2 (2021): 201.

44. J. Amich, Z. Mokhtari, M. Strobel, et al., "Three-Dimensional Light Sheet Fluorescence Microscopy of Lungs to Dissect Local Host Immune-Aspergillus fumigatus Interactions," *mBio* 11 (2020): 02752, https://doi.org/10.1128/mBio.02752-19.

45. M. R. Phillips, S. M. Moore, M. Shah, et al., "A Method for Evaluating the Murine Pulmonary Vasculature Using Micro-Computed Tomography," *Journal of Surgical Research* 207 (2017): 115–122.

46. B. Schneider, K. W. Kopf, E. Mason, M. Dawson, D. Coronado Escobar, and S. M. Majka, "Microcomputed Tomography Visualization and Quantitation of the Pulmonary Arterial Microvascular Tree in Mouse Models of Chronic Lung Disease," *Pulmonary Circulation* 13, no. 3 (2023): e12279.

Supporting Information

Additional supporting information can be found online in the Supporting Information section.